THE ASTROPHYSICAL JOURNAL, 402:605–622, 1993 January 10

MODEL SCATTERING ENVELOPES OF YOUNG STELLAR OBJECTS. II. INFALLING ENVELOPES

BARBARA A. WHITNEY AND LEE HARTMANN
Harvard-Smithsonian Center for Astrophysics, 60 Garden Street, Cambridge, MA 02138
Received 1992 June 2; accepted 1992 July 14

ABSTRACT

We present scattered light images for models of young stellar objects surrounded by dusty envelopes. The envelopes are assumed to have finite angular momentum and are falling in steady flow onto a disk. The model envelopes include holes, such as might be created by energetic bipolar flows. We calculate images using the Monte Carlo method to follow the light scattered in the dusty envelope and circumstellar disk, assuming that the photons originate from the central source. Adopting typical interstellar medium dust opacities and expected mass infall rates for protostars $\dot{M} \sim 10^{-6}\ M_{\odot}\ \mathrm{yr}^{-1}$, we find that detectable amounts of optical radiation can escape from envelopes falling into a disk as small as $\sim$10–100 AU, depending upon the viewing angle and the size of the bipolar flow cavity. The models explain general features of polarization maps of many young stellar objects. In particular, parallel polarization patterns ("polarization disks") can be produced by multiple scattering effects very simply in envelopes and do not require large-scale disk structure. We suggest that the extended optical and near-IR light observed around several young stars is scattered by dusty infalling envelopes rather than disks.

Subject headings: accretion, accretion disks — circumstellar matter — dust, extinction — ISM: jets and outflows — radiative transfer — stars: pre–main-sequence

1. INTRODUCTION

The current picture of star formation envisages the collapse of a rotating, dusty molecular cloud to a star plus disk system, followed by a much longer phase in which the disk either slowly accretes onto the central star or is otherwise dispersed (e.g., Shu, Adams, & Lizano 1987). The heavily extincted sources in star-forming regions are generally identified with the first, "protostellar" phase, while the optically visible T Tauri stars are thought to be in the second, "disk-clearing" phase (Adams, Lada, & Shu 1987). Generally these phases are taken to be distinct, but there are good reasons to expect a certain amount of overlap. In particular, the powerful bipolar outflows associated with the earliest stages of star formation (Edwards, Ray, & Mundt 1991) may clear out lines of sight through the infalling envelope, rendering the central object optically visible.

This picture implies that some objects identified as T Tauri stars may actually be "protostars," in the sense that a substantial amount of mass is still falling onto the circumstellar disk, material which will eventually accrete through the disk onto the central star. The spectral energy distributions at wavelengths longward of 300 μm of some of the brightest T Tauri stars are the same as for embedded sources, which suggests that these T Tauri stars have infalling envelopes (Barsony & Kenyon 1992). Specific objects have been suggested to have substantial remnant dusty envelopes, for example, HL Tau (Beckwith et al. 1989; Grasdalen et al. 1989) and several of the FU Orionis objects (Kenyon & Hartmann 1991).

To investigate potential observational signatures of infalling matter, we present in this paper scattered light images of model dusty envelopes. We are motivated in part by the results of Paper I in this series (Whitney & Hartmann 1992) in which we showed that geometrically thin disks around young stars at the distances of the nearest star-forming regions will be extremely difficult to detect in scattered light. Our results suggested that the reflection nebulae of many young stellar objects must generally arise in dusty envelopes subtending large solid angles as seen from the central source. In this paper we discuss the general behavior of such scattering envelopes and compare to observations of R Mon and T Tau.

2. CALCULATIONS

2.1. *Overview*

The standard model of star formation presumes that a quasi-static cold molecular cloud core eventually collapses in nearly free-fall to a stellar core and disk (e.g., Larson 1969, 1972; Shu 1977; Terebey, Shu, & Cassen 1984; Adams et al. 1987). Detection of a young stellar object requires some central luminosity, which in turn probably implies that a substantial amount of the original envelope mass has already fallen in to form a protostellar or stellar core. We therefore assume that the remnant dusty envelope is in free-fall. In principle, the outer regions of the parent cloud could remain in static equilibrium while the inner regions have fallen in (Larson 1972; Shu 1977), but we neglect the outer region to avoid extra parameters.

In this paper we adopt a specific model for the envelope density distribution, namely the rotating free-fall collapse model of Ulrich (1976) and Cassen & Moosman (1981), which is the inner limit of the Terebey et al. (1984) calculations. Although this assumption is clearly restrictive, it has the advantage that the models are physically possible, if not also plausible. Alternative ad hoc density distributions may be able to model observations as well, but then the physical implications of such models remain unclear. The requirement of finite angular momentum appears to be supported by the apparent ubiquity of circumstellar disks around T Tauri stars (Strom et al. 1989; Beckwith et al. 1990).

We also introduce holes in the dusty envelopes conceptually evacuated by bipolar flows. Such outflows appear to be common among even the most heavily extincted young stellar objects (Terebey, Vogel, & Myers 1989; Heyer et al. 1987). The

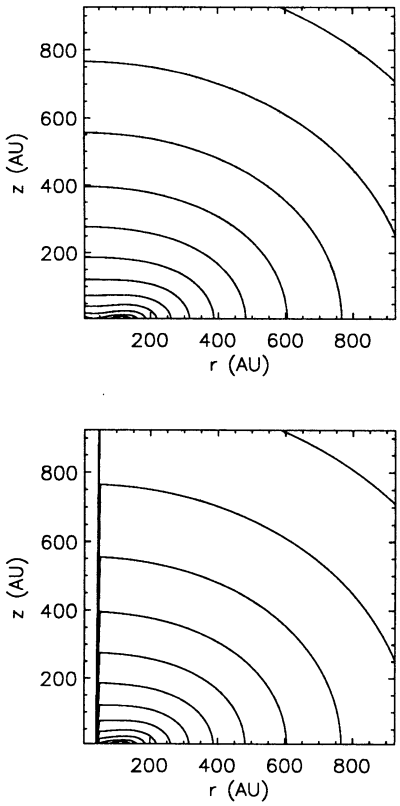

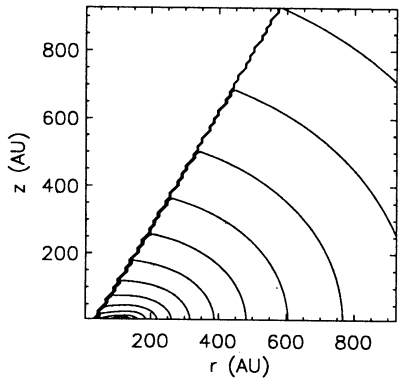

FIG. 1.—Isodensity contours for a collapsing cloud with initially uniform rotation. The centrifugal radius, r_c, is 100 AU. All material from the envelope is instantaneously falling to the disk inside of r_c. Two of the panels show the same density distribution but with holes carved out. The hole shape in the top right panel is a streamline for particles falling in from a direction $\mu_0 = 0.87$. The hole in the bottom panel has a cylindrical radius of 50 AU.

specific geometries of these outflows are somewhat uncertain, but it is clear that the observed momentum fluxes are sufficient to punch holes quickly in the surrounding envelope (Chevalier 1983). In our models we assume that the flows have been present for long enough ($> 10^3$ yr) to evacuate the envelope in the inner region of interest.

2.2. *Model Density Distribution*

We assume that the dusty envelope falls in at a steady rate, over a region of maximum radius $r_{\max} = 1.1 \times 10^4$ AU, which is the radius that encompasses 1 $M_\odot$ in a hydrostatic isothermal spherical cloud, with a typical sound speed $c_s = 0.2$ km s^{-1} (Shu 1977). The exact outer boundary is not very significant for our models, since most of the scattering occurs at much smaller scales.

At small radial distances the angular momentum of the infalling material becomes important. The inner limit of the Terebey et al. (1984) collapse model for a slowly rotating, isothermal, spherical cloud corresponds to the density distribution derived by Ulrich (1976) and Cassen & Moosman (1981) for steady free-fall of a cloud that is initially in uniform angular rotation out to a large distance. In this model, particles fall along parabolic orbits toward the central object, which is assumed to contain most of the mass, and stop when they encounter the disk. The streamlines for the gas particles in a meridional plane are given by the equation

$$\mu_0^3 + (r/r_c - 1)\mu_0 - (r/r_c)\mu = 0 \qquad (1)$$

(Ulrich 1976), where r is the radial distance from force center, $\mu = \cos\theta$ is angle between the radius vector to the particle and the polar axis, $\mu_0 = \mu(r \to \infty)$, and r_c is the "centrifugal radius." Material near the poles has relatively little angular momentum and lands near the central star; at larger angles from the polar axis, gas falls onto the disk at larger distances. Material falling in nearly along the plane of the disk lands just interior to r_c (see Cassen & Moosman 1981). For all orbits, $\mu_0 \geq \mu \geq 0$.

Assuming steady mass infall from an initially spherical cloud, the density distribution for this model is given by

$$\rho = \frac{\dot{M}}{4\pi}\left(\frac{GM}{r_c^3}\right)^{-1/2}\left(\frac{r}{r_c}\right)^{-3/2}\left(1 + \frac{\mu}{\mu_0}\right)^{-1/2}\left(\frac{\mu}{\mu_0} + \frac{2\mu_0^2 r_c}{r}\right)^{-1} \qquad (2)$$

(Ulrich 1976; Cassen & Moosman 1981), where $\dot{M}$ is the mass infall rate and M is the central stellar mass. At distances $r \gg r_c$ the density distribution is essentially spherically symmetric and falls off with radius as $\rho \propto r^{-3/2}$, as expected for steady spherical mass accretion at the free-fall velocity $v \propto r^{-1/2}$. In the vicinity of $r \sim r_c$ the density distribution changes character and becomes flattened (see also Terebey et al. 1984). For $r \ll r_c$, the angle-averaged density varies as $r^{-1/2}$ because much of the infalling matter lands on the outer regions of the disk rather than the star. The isodensity contours for the inner region of this model are shown in Figure 1. The density distribution (2) exhibits a singularity at $\theta = 90°$, $r = r_c$ where streamlines converge, but this has no practical importance to our modeling. The buildup of density in a ringlike structure is a real effect (Cassen & Moosman 1981), and the singularity is avoided in the choice of the density grid mapping.

At large distances ($r > 10^4$ AU), the true density distribution departs from $\rho \propto r^{-3/2}$, in part because the envelope mass is not negligible in comparison with the central mass (Shu 1977). We neglect this complication, which in our case will affect only the optical depth at regions $\sim 10^4$ AU, and thus is almost equivalent to adding additional foreground extinction. Equations (1) and (2) also assume that the disk mass can be neglected.

We introduce polar holes into the density distribution to account for the effect of bipolar flows. The dust opacity in the high velocity outflow is much smaller than in the infalling envelope, so we consider the hole to be evacuated. To minimize the number of parameters, we assume that the wind has blown completely through the envelope (Chevalier 1983). We consider two types of bipolar wind-driven holes. The first assumes

that the hole is confined within the meridional component of a streamline defined in equation (1), setting $\mu_0 = \cos \theta_{max}$. Thus, at large distances $r \gg r_c$, the hole is an evacuated cone. The other type of hole is cylindrical, oriented along the rotation axis, and is motivated by the highly collimated jets seen emanating from some pre–main-sequence objects. Figure 1 shows the density distributions with these hole shapes. For the streamline hole, we let $\mu_0 = 0.87$, and for the cylindrical hole we take a cylindrical radius of 50 AU.

The model is completed by the addition of a geometrically thin, optically thick disk. The disk has little effect on the model results presented here as long as it is optically thick at visual and near-IR wavelengths, which is strongly supported by observations (Strom et al. 1989; Beckwith et al. 1990). To avoid introducing additional parameters, we take the outer radius of the disk to be r_c, noting that angular momentum transfer in the disk could cause it to spread beyond this point (Cassen & Moosman 1981; Lin & Pringle 1990). The inner radius of the disk is the stellar radius, R_*, and the disk thickness h is about 0.1 R_* (4 scale heights) as in Paper I.

2.3. *Dust Parameters*

As in Paper I, we adopt dust parameters from the Mathis, Rumpl, & Nordsieck (1977; hereafter MRN) gas and dust mixture, for which White (1979) has calculated polarization properties. MRN has opacity $\kappa = 250$ cm^2 g^{-1}, albedo $\omega = 0.5$, scattering asymmetry parameter $g = 0.45$, and maximum polarization $p_{max} = 0.5$ (White 1979) at $\lambda = 5500$ Å. The asymmetry parameter, used in the Henyey-Greenstein phase function for scattering, approximates the forward-throwing properties of the dust. Typically $\omega \sim g \sim 0.5$ if the wavelength of light is about the same size as the grains (Witt 1989). In the near IR, MRN grains are small compared to the wavelength of light, so the scattering phase function approaches that of the small particle limit. The albedo and opacity drop as the wavelength increases. At the J band, 1.25 μm, the opacity decreases to $\kappa = 75$ cm^2 g^{-1}, and the albedo is $\omega = 0.4$. At K, 2.2 μm, the opacity is about 25 cm^2 g^{-1}, the albedo falls to $\omega = 0.2$, and the polarization increases to $p_{max} \approx 0.95$.

We use two grain types in our models. The type representing visual wavelengths has albedo $\omega = 0.5$, scattering asymmetry parameter $g = 0.45$, and maximum polarization $p_{max} = 0.5$, and we denote this as F for forward-throwing high-albedo grains. This scattering phase function has 8 times as much flux going into the forward direction as at 90° and continues to decrease in the backscattering directions. A plot of the phase function is shown in Paper I. The type representative of infrared scattering has $\omega = 0.2$, $p_{max} = 0.77$, and the scattering phase function for Rayleigh scattering (Chandrasekhar 1960). Here twice as much flux scatters into the forward direction as that at 90°, and the function is symmetric about the 90° scattering angle. These grains are denoted as R and represent low-albedo Rayleigh scattering grains. Pendleton, Tielens, & Werner (1990) argue that grains may be larger in dark clouds, in which case we can use the F grain models for the IR.

2.4. *Radiative Transfer Calculations*

Paper I outlines the methods used to solve the radiative transfer problem. We assume that all of the scattered light from the envelope and disk originates at a central source, which is taken to be a sphere of uniform surface brightness. The Monte Carlo method follows the multiple scattering of the photons, including polarization, until they pass through the outer boundary or are absorbed. To produce the image an observer would see viewing the system from angle i measured from the polar axis, we bin the exiting photons into a spatial grid at each of 11 angle bins, centered at $\cos i \equiv \mu = 0.1(n - 1)$, $n = 1, 2, \ldots, 11$.

2.5. *Scaling of Models*

The density distributions of the models employed here have the same form as a function of r/r_c and the streamline of the cavity, denoted by μ_0. Assuming the dust has a fixed albedo and phase function, models can be scaled at the same optical depth. This scaling can be derived by considering the polar optical depth in the absence of wind-driven cavities, calculated by integrating equation (2) along $\mu = 0$.

$$\tau_p = \frac{\kappa \dot{M}}{4\pi (GM)^{1/2}} r_c^{-1/2} \times \{\tan^{-1} [(2x_{min})^{-1/2}] - \tan^{-1} [(2x_{max})^{-1/2}]\} , \quad (3)$$

where $x_{max} = r_{max}/r_c$ and $x_{min} = r_{min}/r_c$. When $x_{min} \ll 1$, as is always the case, and $x_{max} \gg 1$, as is generally the case, the models will have the same optical depths and hence the same scattered light properties if $\kappa \dot{M} M^{-1/2} \propto r_c^{1/2}$. This optical depth will scale with the optical depths at any other viewing angle μ because of the self-similarity of the model density distributions.

3. RESULTS

3.1. *Models without a Wind Cavity*

We begin by presenting results for reference models of dusty infalling envelopes without bipolar cavities (models 1–4). The models were calculated for two values of the parameter γ, where

$$\gamma = \kappa/(250 \text{ cm}^2/\text{g}) \dot{M}/(2 \times 10^{-6} M_\odot \text{ yr}^{-1}) \times [M/(0.5 M_\odot)]^{-1/2} [r_c/(100 \text{ AU})]^{-1/2} , \quad (4)$$

and the two dust scattering types discussed in § 2.3. Table 1 lists the parameters for each model. A radius of $r_c = 100$ AU is consistent with typical disk radii derived by Beckwith et al. (1990) and Adams, Emerson, & Fuller (1990). The mass infall rate of $\dot{M} = 2 \times 10^{-6} M_\odot$ yr^{-1} corresponds to an initial (thermally supported) cloud temperature of 10 K (Shu 1977). These models without cavities have $\gamma < 1$, because the optical depth through the envelope is too high at $\gamma = 1$ for a significant amount of flux to escape. If $\gamma = 1$, the optical depth is greater than 10 along the polar axis, and larger in other directions.

Table 2 summarizes results for the envelopes without holes as a function of inclination. The flux and polarization are summed over a region of the image with a circular diameter of 1600 AU (about 10″ at the distance to the Taurus molecular cloud). The fluxes are normalized to the stellar flux F_*. The total flux F emergent at inclination $\mu = \cos \theta$ is the sum of the unscattered component F_u and the scattered component. Note that F_u is less than $F_* e^{-\tau}$, because the disk obscures part of the star.

The total amount of light which escapes depends on the inclination. Viewing model 1 at an inclination of $\mu = 0$ (edge-on), an observer would detect approximately 1% of the light that would be seen if no envelope or disk were present, while at $\mu = 1$, this fraction is 6.2%. The reason for this difference is the flattening of the density distribution of the envelope due to

TABLE 1

MODEL PARAMETERS

Model	Dust Type[a]	$\kappa\dot{M}M^{-1/2}r_c^{-1/2}$ [b]	Hole Type[c]
1	F	0.3163[c]	No hole
2	R	0.3163	No hole
3	F	0.1	No hole
4	R	0.1	No hole
5	F	1	Streamline
6	R	1	Streamline
7	F	0.3163	Streamline
8	R	0.3163	Streamline
9	F	0.1	Streamline
10	R	0.1	Streamline
11	F	1	Cylindrical
12	R	1	Cylindrical
13	F	0.3163	Cylindrical
14	R	0.3163	Cylindrical
15	F	0.1	Cylindrical
16	R	0.1	Cylindrical

[a] F denotes the high-albedo forward-throwing dust parameters, typcal V-band parameters ($\omega = 0.5$, $p_{max} = 0.5$, $g = 0.45$); the R models use low-albedo Rayliegh scattering typical of the IR ($\omega = 0.2$, $p_{max} = 0.77$). These parameters are described in § 2.3.

[b] In units of $\kappa/(250\ \mathrm{cm^2/g})\dot{M}/(2\times10^{-6}\ M_\odot\ \mathrm{yr}^{-1})[M/(0.5\ M_\odot)]^{-1/2}[(r_c/(100\ \mathrm{AU})]^{-1/2}$ (defined as γ in § 3.1).

[c] The streamline hole has opening angle at large r of $\mu_0 = 0.87$. The cylindrical hole has a cylindrical radius of $1/2r_c$.

rotation, which produces extra extinction near the disk plane (Fig. 1), as indicated by the angle dependence of the optical depth τ through the envelope to the central source (Table 2). At $\mu = 0.1$, τ is equal to 8.9, and the central source is heavily extincted, whereas at $\mu = 1$, $\tau = 3.6$. Note that the direct flux is several orders of magnitude smaller than the scattered flux at high inclination. An optical extinction estimate based on the amount of light escaping from the system would be grossly underestimated if this scattered light were assumed to be direct flux. (The optical depth τ is not calculated precisely to the star at $\mu = 0$ because the line of sight passes through the optically thick disk. We therefore integrate the optical depth through the envelope in a plane above $z = 0$.)

The integrated polarization, presented in Table 2, is defined so that positive polarization is oriented perpendicular to the disk, negative parallel to disk. The amount of polarization is strongly dependent on inclination angle. Maximum polarization occurs at small μ, when the envelope is most asymmetric in appearance, and the direct unpolarized light from the central source is most extinguished. As shown in Table 2, these models have negative polarization. A model with a factor of 10 lower value of γ (not shown here) gives a positive net polarization, because scattering from the equatorial regions dominates.

Images calculated at three different inclinations are shown in Figure 2. The maps have been convolved with a two-dimensional Gaussian point-spread function with a FWHM of 80 AU to reduce fluctuations due to photon statistics. This smoothing is roughly consistent with 0".5 seeing if the object were at the distance of Taurus (160 pc). Seen nearly edge-on (Fig. 2*a*), the object appears very extended, with a dark band across the object, giving the outer contours a characteristic "hourglass" shape. This feature in the outer contours is due to a "shadowing" effect of the type described by Lazareff, Pudritz, & Monin (1990). High-density material in a toroidal pattern scatters or absorbs photons from the central source, shadowing outer regions. As pointed out by Lazareff et al., this effect can produce asymmetric light distributions in regions where the density distribution is not asymmetric. Thus the mere detection of asymmetry in the scattered light at a particular point is *not* proof that the dust is locally asymmetrically distributed. The asymmetry can be produced by structure on much smaller scales.

Polarization maps for models 1–4 are also shown in Figure 2. Many of the maps show a generally centrosymmetric pattern. The vectors are quite large (~25% for the F-grain models, and about twice that for the R-grain models), but none is as large as the maximum polarization for single scattering at 90° (50% for the F-grain models, 77% for the R-grain models). In the higher optical depth models (e.g., model 1) the pattern becomes more elliptical, with smaller polarization along the disk plane. Very few photons reach the equatorial regions directly, instead scattering first in the polar regions. This introduces a parallel component to the polarization which depolarizes the perpendicular component due to single scattering. We will see this effect become more pronounced in the higher optical depth models in § 3.2.

Note that high-polarization vectors (>20%) result in all of these images, even in models 1 and 2, where the smallest optical depth is 3.6. Thus high polarization in itself should not be taken to mean the optical depths are small. It results in this case because the albedo is ≤0.5, so the average number of scatters is small. In Table 5, we tabulate the average number of scatters of the scattered flux (not including the absorbed photons) in all of the models. The average numbers of scatters is usually less than 2.

TABLE 2

ENVELOPES WITHOUT HOLES

	MODELS 1, 2		MODEL 1		MODEL 2		MODELS 3, 4		MODEL 3		MODEL 4	
μ	τ	F_u/F_*	F/F_*	%P	F/F_*	%P	τ	F_u/F_*	F/F_*	%P	F/F_*	%P
0	>20	$\sim10^{-6}$	9.9×10^{-3}	−9.7	1.4×10^{-3}	−23	>5.0	8.1×10^{-3}	8.0×10^{-2}	−2.9	2.7×10^{-2}	−6.5
0.1	8.9	$\sim10^{-4}$	1.04×10^{-2}	−9.4	1.5×10^{-3}	−23	2.8	2.6×10^{-2}	1.02×10^{-1}	−2.1	4.7×10^{-2}	−3.4
0.2	7.2	4×10^{-4}	1.16×10^{-2}	−8.0	1.9×10^{-3}	−17	2.3	5.1×10^{-2}	1.33×10^{-1}	−1.3	7.28×10^{-2}	−1.9
0.3	6.2	1.0×10^{-3}	1.38×10^{-2}	−6.8	2.8×10^{-3}	−11	2.0	7.71×10^{-2}	1.67×10^{-1}	−0.7	1.01×10^{-1}	−1.2
0.4	5.5	2.2×10^{-3}	1.70×10^{-2}	−5.0	4.3×10^{-3}	−6.9	1.7	1.04×10^{-1}	2.02×10^{-1}	−0.3	1.30×10^{-1}	−0.7
0.5	5.0	3.9×10^{-3}	2.15×10^{-2}	−3.6	6.4×10^{-3}	−4.3	1.6	1.33×10^{-1}	2.39×10^{-1}	−0.2	1.60×10^{-1}	−0.4
0.6	4.6	6.4×10^{-3}	2.73×10^{-2}	−2.4	9.5×10^{-3}	−2.6	1.5	1.63×10^{-1}	2.79×10^{-1}	−0.0	1.91×10^{-1}	−0.3
0.7	4.3	9.4×10^{-3}	3.42×10^{-2}	−1.4	1.31×10^{-2}	−1.5	1.4	1.95×10^{-1}	3.19×10^{-1}	0.0	2.25×10^{-1}	−0.2
0.8	4.0	1.36×10^{-2}	4.30×10^{-2}	−0.8	1.79×10^{-2}	−0.9	1.3	2.29×10^{-1}	3.60×10^{-1}	0.0	2.61×10^{-1}	−0.0
0.9	3.8	1.87×10^{-2}	5.29×10^{-2}	−0.3	2.37×10^{-2}	−0.4	1.2	2.67×10^{-1}	4.06×10^{-1}	0.0	3.00×10^{-1}	−0.0
0.975	3.6	2.35×10^{-2}	6.17×10^{-2}	−0.2	2.90×10^{-2}	−0.1	1.1	2.97×10^{-1}	4.42×10^{-1}	0.0	3.32×10^{-1}	0

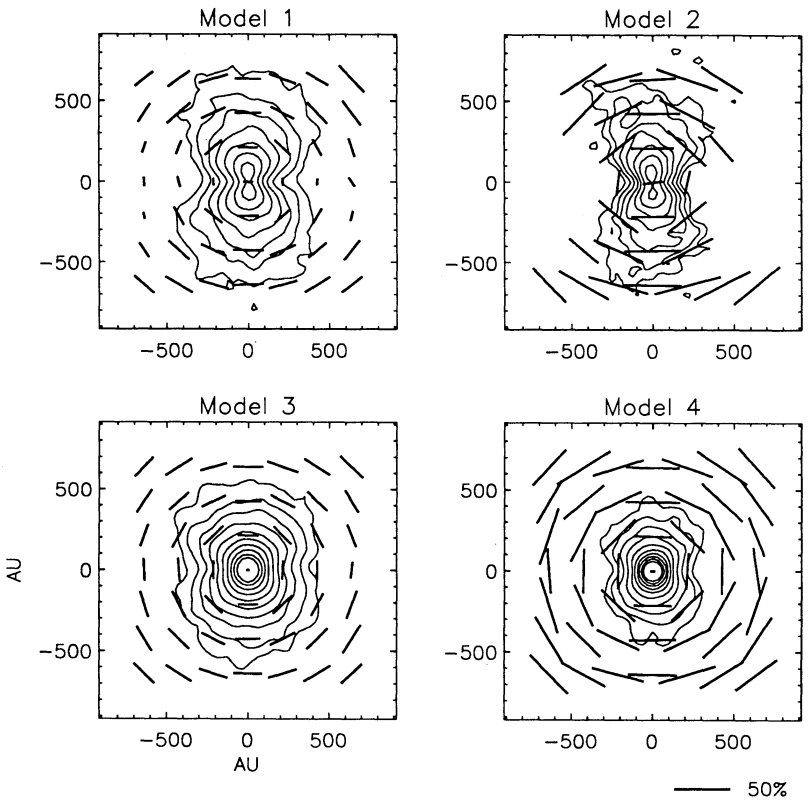

FIG. 2*a*

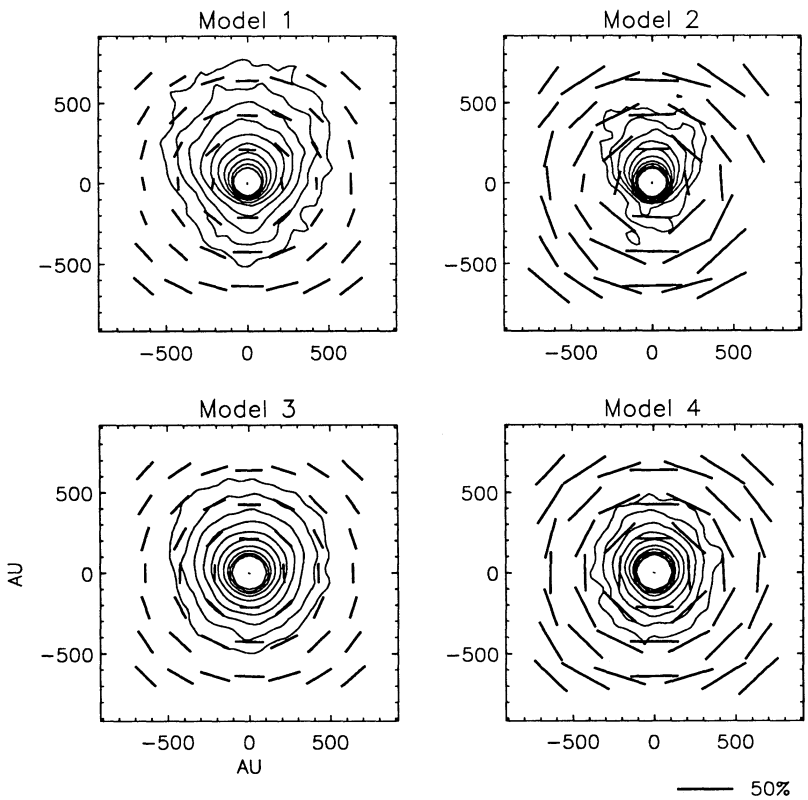

FIG. 2*b*

FIG. 2.—(*a*) Images and polarization maps of an envelope (and disk) illuminated by a central source at an inclination of $\mu = 0$. The top two panels are models with higher optical depth; the left panels are models with forward-throwing high-albedo scattering parameters, and the right panels have isotropic low-albedo parameters (see Table 1 and § 2.3). Images are convolved with a Gaussian point-spread function of 80 AU and normalized to the peak flux. Contours are spaced logarithmically at intervals of 0.5 mag. The lowest contours of each image are 5×10^{-2}, 5×10^{-2}, 5×10^{-3}, and 5×10^{-3}, for models 1, 2, 3, and 4, respectively. (*b*) Same as Fig. 2*a*, with $\mu = 0.6$. The lowest contours are 2×10^{-3}, 1×10^{-3}, 5×10^{-4}, and 2.5×10^{-4}, for models 1, 2, 3, and 4, respectively. (*c*) Same as Fig. 2*a*, with $\mu = 0.9$. The lowest contours are 1×10^{-3}, 2.5×10^{-4}, 2×10^{-4}, and 1×10^{-4}, for models 1, 2, 3, and 4, respectively.

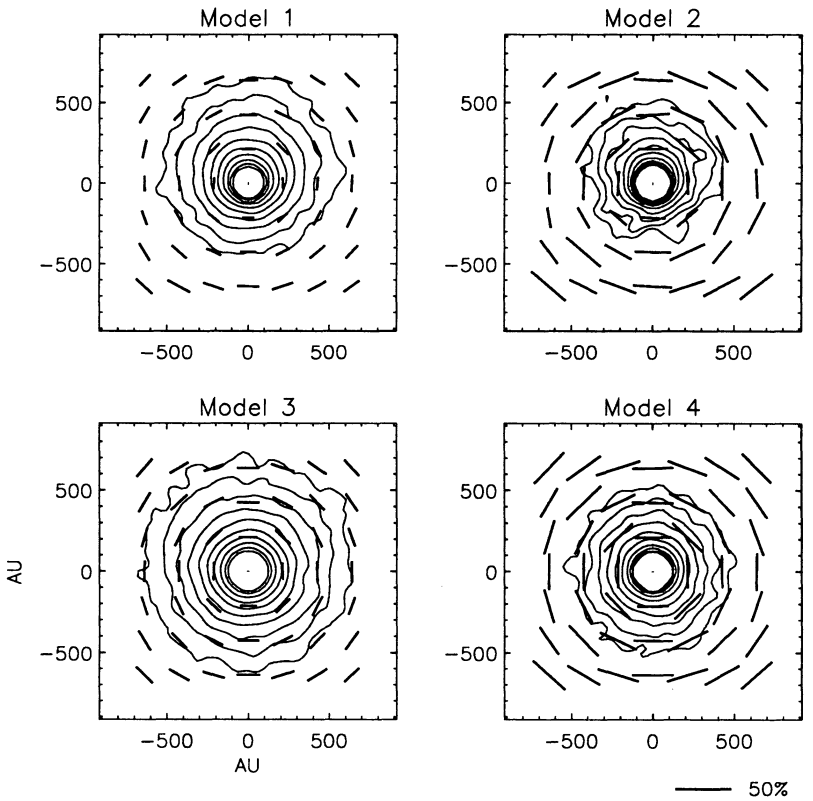

FIG. 2c

Comparing the different grain properties and optical depths at a given inclination, we see that the R-type grains scatter less light and give higher polarization than the F-type for the obvious reasons of lower albedo and higher p_{max}. From examining Table 2, the integrated scattered flux ($F/F_* - F_u/F_*$) in model 1 is about 7 times that in model 2. The scattered flux in model 3 is about 4 times that in model 4. In the limit of small optical depth, where the scattering is mostly single, the ratio of scattered light between F and R models will be roughly the ratio of the albedos (though it depends on the dominant scattering angle). Because less flux is scattered in the R-grain models (models 2 and 4), the images are smaller than in the F-grain models (models 1 and 3) for a given contour level. At lower optical depth (models 3 and 4) the images become less asymmetric because photons can travel farther in the equatorial direction, making the image more diffuse.

The integrated polarization of model 2 is over twice that of model 1 at high inclination. This reflects the fact that p_{max}, the maximum polarization for single scattering, of model 1 is a factor of 1.54 times bigger in the low-albedo models, and that the average number of scatters in model 2 is less. Also, the singly scattered photons, which dominate the low-albedo flux, arise in the polar regions, giving a more asymmetric distribution of the scattered light (as can be seen in Fig. 2*a*) and thus a higher polarization. At lower inclinations, where the optical depths to the source are lower, the effect is less pronounced, and in fact the ratio of the polarizations between the two models is smaller than the ratio of the values of p_{max}. At low optical depth, the integrated polarization is less because the central unpolarized source becomes brighter, and the scattering is more symmetric.

3.2. *Models with Streamline Wind Cavity*

In models 5–10 we introduce bipolar cavities which follow streamlines of $\mu_0 = 0.87$ (this choice of μ_0 is somewhat arbitrary). As expected, much more optical light escapes in this case. Models 7–10 (the bottom four panels in Fig. 3) have the same parameters as models 1–4, with the addition of the hole. Models 5 and 6 have a higher value of $\gamma(\kappa\dot{M}M^{-1/2}r_c^{-1/2})$, shown in Table 1. If MRN dust properties apply, model 10 can be thought of as the K image of an object whose V image corresponds to model 5.

The results are shown in Table 3 and Figure 3. Comparing models 7–8 to models 1–2, we see more flux escaping and less polarization. However, at higher optical depth, as in models 5–6, the polarization can be large over a wide range of inclination. Also interesting is the rotation of position angle by 90° between models 7–8 and models 9–10. The reason is simple: In the high optical depth models, single scattering in the envelope dominates the polarization so the position angle is parallel to the disk plane; in the low optical depth models, more flux scatters in the equatorial region so the position angle is perpendicular to the disk plane. The models without holes also show a 90° rotation with wavelength but at lower optical depths than the models shown here, because the envelope is filled in at the poles, giving more scattering in this region.

The intensity maps in Figure 3 show fan-shaped structure which roughly follows the outlines of the wind-excavated cavities, especially at high optical depth. For $\mu \geq 0.4$ the surface brightness contours no longer show the lower cavity, because of the large optical depth through the envelope. This is true for both grain types; i.e., the dominant effect is obscuration by a large amount of dust, not the amount of forward-throwing in

TABLE 3

ENVELOPES WITH STREAMLINE HOLES

	Models 5, 6		Model 5		Model 6	
μ	τ	F_u/F_*	F/F_*	%P	F/F_*	%P
0	>50	$<10^{-6}$	4.7×10^{-4}	−12	1×10^{-4}	−29
0.1	24	$<10^{-6}$	5.0×10^{-4}	−12	1×10^{-4}	−29
0.2	19	$<10^{-6}$	5.7×10^{-4}	−11	1×10^{-4}	−30
0.3	15	$<10^{-6}$	6.7×10^{-4}	−11	1×10^{-4}	−31
0.4	13	$<10^{-6}$	8.6×10^{-4}	−12	2×10^{-4}	−32
0.5	11	$<10^{-5}$	1.2×10^{-3}	−13	3×10^{-4}	−32
0.6	9.1	$\sim 10^{-4}$	1.9×10^{-3}	−14	5×10^{-4}	−29
0.7	7.3	$\sim 6 \times 10^{-4}$	4.0×10^{-3}	−13	1.5×10^{-3}	−19
0.8	4.6	1.66×10^{-2}	2.95×10^{-2}	−5	2.00×10^{-2}	−3.6
0.9	0	8.02×10^{-1}	9.58×10^{-1}	0	8.44×10^{-1}	−0.0
0.975	0	9.63×10^{-1}	1.162	0	1.01	0.0
	Models 7, 8		Model 7		Model 8	
μ	τ	F_u/F_*	F/F_*	%P	F/F_*	%P
0	>20	1×10^{-5}	1.95×10^{-2}	−2.7	4.8×10^{-3}	−9.5
0.1	7.5	2×10^{-4}	2.03×10^{-2}	−2.7	5.0×10^{-3}	−9.1
0.2	5.9	1.4×10^{-3}	2.28×10^{-2}	−2.1	6.5×10^{-3}	−7.3
0.3	4.8	4.5×10^{-3}	2.80×10^{-2}	−1.4	9.9×10^{-3}	−5.3
0.4	4.1	1.00×10^{-2}	3.62×10^{-2}	−0.8	1.61×10^{-2}	−3.2
0.5	3.4	2.09×10^{-2}	5.08×10^{-2}	−0.4	2.77×10^{-2}	−2.1
0.6	2.9	4.01×10^{-2}	7.46×10^{-2}	−0.5	4.84×10^{-2}	−1.5
0.7	2.3	7.98×10^{-2}	1.22×10^{-1}	−0.6	9.03×10^{-2}	−0.9
0.8	1.5	2.15×10^{-1}	2.72×10^{-1}	−0.4	2.32×10^{-1}	−0.4
0.9	0	8.59×10^{-1}	1.02	0.2	9.04×10^{-1}	0.0
0.975	0	9.64×10^{-1}	1.15	0	1.02	0.0
	Models 9, 10		Model 9		Model 10	
μ	τ	F_u/F_*	F/F_*	%P	F/F_*	%P
0	>5	1.27×10^{-2}	8.1×10^{-2}	3.4	3.2×10^{-2}	3.1
0.1	2.4	4.15×10^{-2}	1.11×10^{-1}	2.5	6.2×10^{-2}	1.9
0.2	1.9	8.00×10^{-2}	1.54×10^{-1}	2.1	1.01×10^{-1}	1.3
0.3	1.5	1.23×10^{-1}	2.01×10^{-1}	1.8	1.46×10^{-1}	0.9
0.4	1.3	1.69×10^{-1}	2.51×10^{-1}	1.5	1.93×10^{-1}	0.8
0.5	1.1	2.25×10^{-1}	3.12×10^{-1}	1.2	2.50×10^{-1}	0.6
0.6	0.91	2.92×10^{-1}	3.83×10^{-1}	0.9	3.19×10^{-1}	0.4
0.7	0.73	3.82×10^{-1}	4.76×10^{-1}	0.6	4.11×10^{-1}	0.2
0.8	0.46	5.44×10^{-1}	6.47×10^{-1}	0.3	5.78×10^{-1}	0.1
0.9	0	8.92×10^{-1}	1.03	0.2	9.37×10^{-1}	0.1
0.975	0	9.62×10^{-1}	1.10	0	1.01	0

the scattered phase function. The disk extends only to a projected radius of 100 AU in Figure 3 and is not responsible for occulting the lower cavity.

Lazareff et al. (1990) produced surface brightness maps of similar appearance, in which the "hourglass" shape of the scattered light distribution was produced primarily by a large disk ($\sim$700 AU) of finite thickness ($z/r \sim \frac{1}{4}$). However, their images are somewhat misleading because the surface brightness of the envelope is extremely faint in comparison with the central light source (Paper I). In our models, the envelope strongly obscures the central star, making the envelope relatively brighter and hence much easier to detect observationally. Moreover, *the toroidal structure is due entirely to the density distribution of the envelope, not the disk.*

The polarization maps show more features than the models with no hole except at low optical depth (models 9–10) where the pattern is nearly centrosymmetric. For $\mu = 0$ (Fig. 3*a*), the models show a pronounced decrease in the magnitude of polarization along the rotational axis. This is because there is no material along the rotational axis to scatter light at a 90° angle, the angle which produces the most polarization. The patterns in the disk plane can either be parallel to the disk plane (model 5), perpendicular but decreased compared to other vectors (model 7), or the same size as others (model 9). The parallel pattern of vectors in model 5 is a feature which has been seen in many young stellar objects (see § 4.2). The optical depths through the envelope in this region are $\sim$50, so very few photons reach these regions directly. Instead, they scatter in the polar regions first and then down to this region before scattering to the observer. The surviving polarization in these multiply scattered photons is perpendicular to the scattering angles, or parallel to the disk plane. This is similar to the idea proposed by Bastien & Ménard (1988, 1990), except they attribute the parallel vectors to multiple scattering in a large disk instead of an envelope.

At lower inclinations ($\mu > 0.6$) the model maps show high polarization along the rotation axis, because of the near 90° scattering off the hole walls. The same scattering angle occurs in the upper lobe at the far side of the wall as in the lower lobe on the near side. In some of the models, the polarization in the

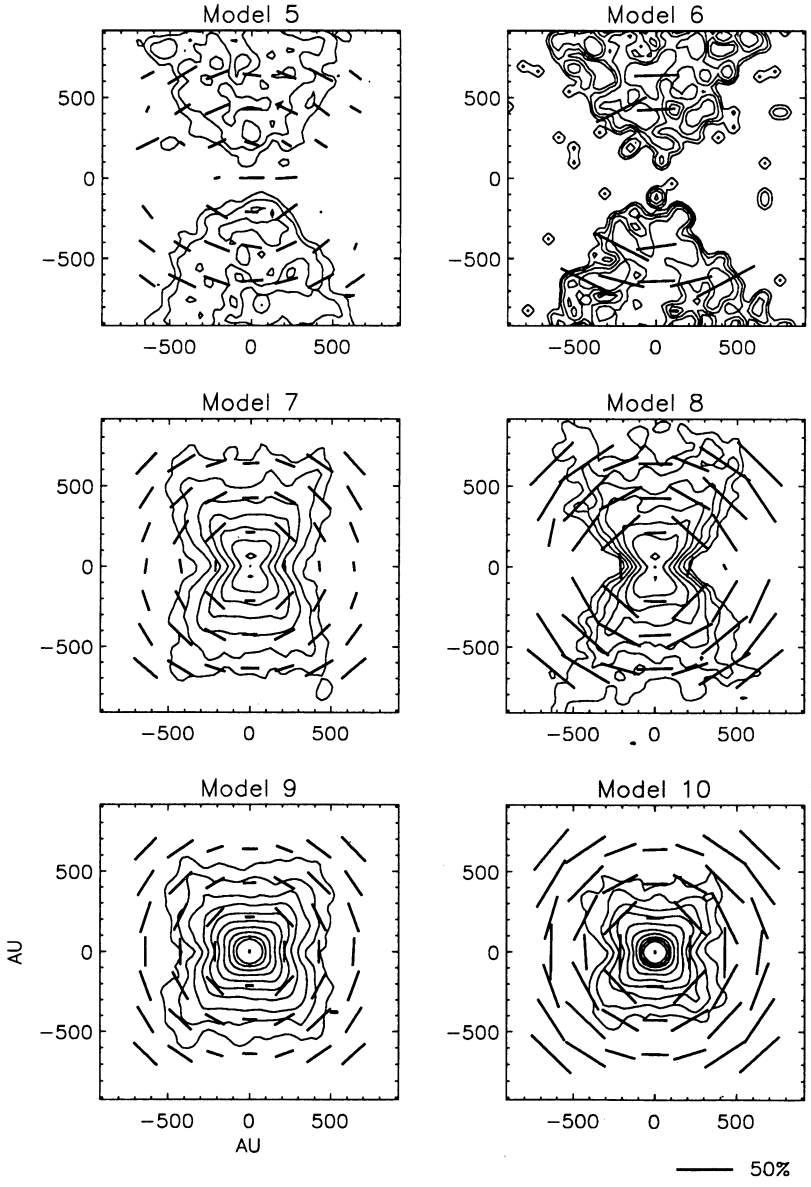

FIG. 3*a*

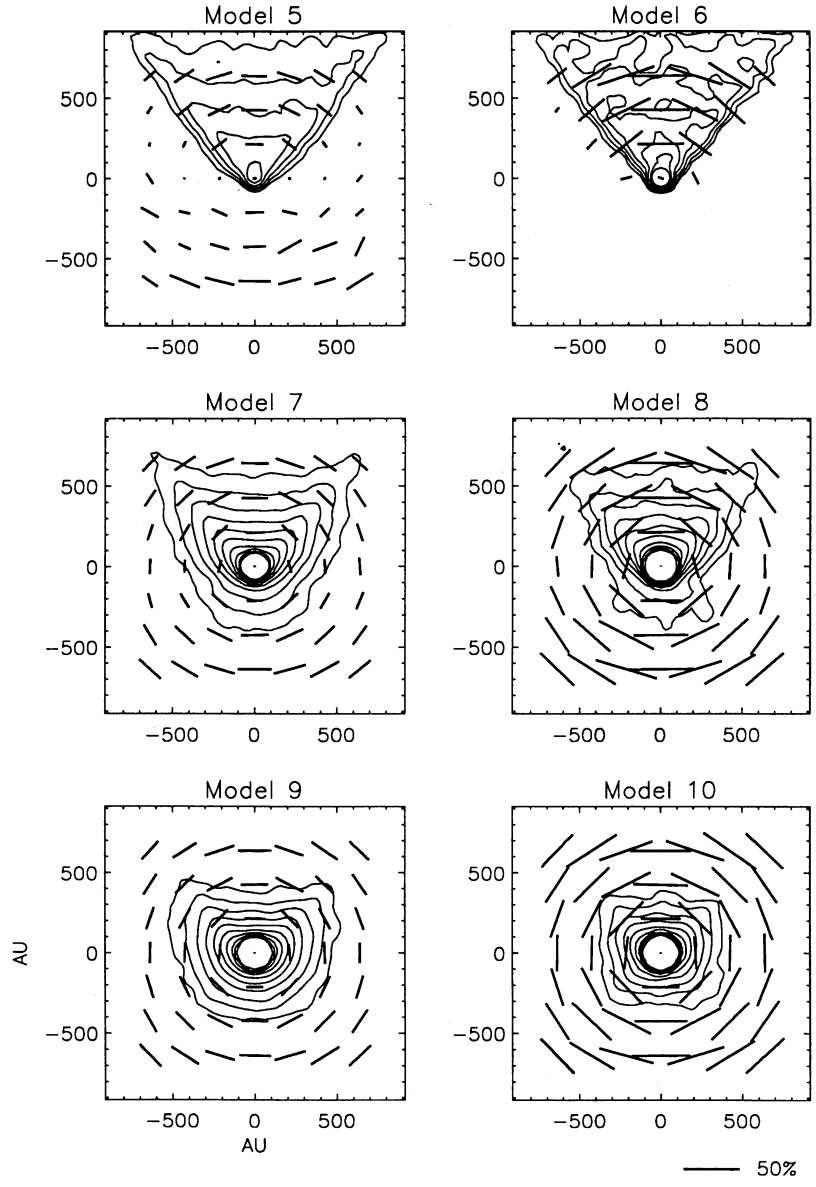

FIG. 3*b*

FIG. 3.—(*a*) Images and polarization maps of an envelope with evacuated polar regions, for an inclination $\mu = 0$. The cavity shape is that of a streamline at $\mu_0 = 0.87$ (see Fig. 1, § 2.2, and § 3.2). As in Fig. 2, the leftside models use *F*-type grain parameters, and the right use *R*-type; going from top to bottom, the optical depth decreases (Table 1). Images are convolved with a Gaussian point-spread function of 80 AU and normalized to the peak flux. Contours are spaced by 0.5 mag, or a factor of 1.58. The lowest contours of each image are 3×10^{-1}, 1×10^{-1}, 6×10^{-2}, 6×10^{-2}, 4×10^{-3}, and 3×10^{-3}, for models 5, 6, 7, 8, 9, and 10, respectively. (*b*) Same as Fig. 3*a*, with $\mu = 0.6$. The lowest contours are 1×10^{-1}, 2×10^{-2}, 1.5×10^{-3}, 4×10^{-4}, 4×10^{-4}, and 2×10^{-4}, for models 5, 6, 7, 8, 9, and 10, respectively. (*c*) Same as Fig. 3*a*, with $\mu = 0.9$. The lowest contours are 1×10^{-4}, 5×10^{-5}, 1×10^{-4}, 5×10^{-5}, 1×10^{-4}, and 5×10^{-5} for models 5, 6, 7, 8, 9, and 10, respectively.

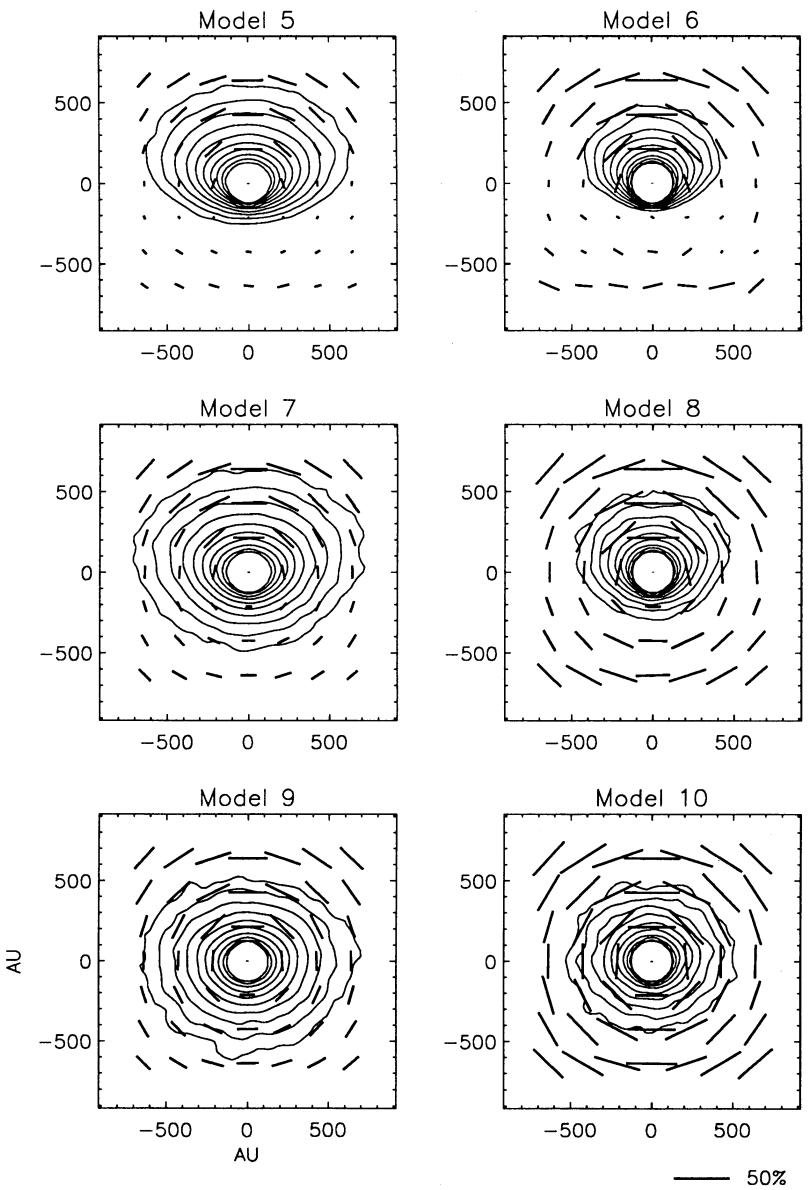

FIG. 3c

lower lobe is higher than that of the upper lobe (Fig. 3*b*, model 7, Fig. 2*b*, models 1 and 3), at intermediate inclinations. This is not the case in the *R*-type grain models (Fig. 3*b*, model 8, Fig. 2*b*, models 2 and 4) and reflects the difference in the scattering phase functions. In the *F*-grain models, the scattered flux is weighted toward smaller angles, which in the upper lobe will be closer to 0° (the near side of the wall) and give less polarization, and in the lower lobe will be closer to 90° and give higher polarization. This feature allows us to distinguish grain types: In an axisymmetric distribution of dust illuminated by a central source and inclined to our line of sight, if the faint lobe is more polarized than the bright lobe, a possible explanation is that the grains are forward throwing. The major difference in the two lobes is that the scattered flux in the lower lobe is extincted by the envelope, but this does not change its polarization significantly.

Finally, the null patterns along or below the equatorial plane are very pronounced at high optical depths and intermediate inclinations. This is presumably a cancellation of parallel and perpendicular vectors, since the line of sight in the equatorial band passes through the diffuse outer envelope.

3.3. *Models with Cylindrically Shaped Cavity*

The wind hole shape here is chosen to be a cylinder of radius $r_c/2$. Otherwise it has the same parameters as the streamline hole models. The results are shown in Table 4 and Figure 4. Except at large optical depth (models 11–12), the images resemble the cases without a hole (models 1–4). This is because the effect of the cylindrical hole is to lower the overall optical depth, while maintaining the flattened density structure of the envelope. The high optical depth models give very elliptical polarization maps (model 11, Figs. 4*a*, *b*, *c*). At low inclination and high optical depth (model 11, Fig. 4*c*), the polarization map has a very interesting shape: The vectors in the lower lobe are mostly parallel to the disk plane; in the upper lobe they are mostly perpendicular to the disk plane, except along the polar

TABLE 4

ENVELOPED WITH CYLINDRICAL HOLES

	MODELS 11, 12		MODEL 11		MODEL 12	
μ	τ	F_u/F_*	F/F_*	%P	F/F_*	%P
0	>50	$<10^{-6}$	4×10^{-4}	−20	5×10^{-5}	∼−50
0.1	22	$<10^{-6}$	4×10^{-4}	−20	6×10^{-5}	∼−50
0.2	17	$<10^{-6}$	4×10^{-4}	−19	6×10^{-5}	∼−45
0.3	14	$<10^{-6}$	5×10^{-4}	−18	7×10^{-5}	∼−45
0.4	12	$\sim 10^{-6}$	6×10^{-4}	−15	8×10^{-5}	∼−40
0.5	11	$\sim 10^{-5}$	8×10^{-4}	−14	1×10^{-4}	∼−30
0.6	9.8	$\sim 4 \times 10^{-5}$	1.0×10^{-3}	−11	2×10^{-4}	−20
0.7	8.8	1×10^{-4}	1.5×10^{-3}	−8	3×10^{-4}	−13
0.8	7.8	3×10^{-4}	2.1×10^{-3}	−5	6×10^{-4}	−6
0.9	6.6	1.3×10^{-3}	3.8×10^{-3}	−3	1.6×10^{-3}	−2
0.975	0	1.70×10^{-2}	2.13×10^{-2}	−0.6	1.77×10^{-2}	−0.2
	MODELS 13, 14		MODEL 13		MODEL 14	
μ	τ	F_u/F_*	F/F_*	%P	F/F_*	%P
0	>15	2×10^{-5}	2.68×10^{-2}	−9.5	5.9×10^{-3}	−23
0.1	7.0	5×10^{-4}	2.78×10^{-2}	−9.1	6.5×10^{-3}	−21
0.2	5.4	2.4×10^{-3}	3.12×10^{-2}	−7.6	8.7×10^{-3}	−15
0.3	4.5	5.9×10^{-3}	3.72×10^{-2}	−6.1	1.26×10^{-2}	−9.8
0.4	3.9	1.20×10^{-2}	4.65×10^{-2}	−4.3	1.92×10^{-2}	−5.8
0.5	3.5	2.02×10^{-2}	5.90×10^{-2}	−3.0	2.81×10^{-2}	−3.8
0.6	3.1	3.22×10^{-2}	7.59×10^{-2}	−2.0	4.09×10^{-2}	−2.1
0.7	2.8	4.81×10^{-2}	9.73×10^{-2}	−1.2	5.80×10^{-2}	−1.3
0.8	2.5	7.11×10^{-2}	1.27×10^{-1}	−0.8	8.20×10^{-2}	−0.7
0.9	2.1	1.13×10^{-1}	1.76×10^{-1}	−0.5	1.26×10^{-1}	−0.4
0.975	0	2.26×10^{-1}	3.00×10^{-1}	−0.2	2.41×10^{-1}	−0.2
	MODELS 15, 16		MODEL 15		MODEL 16	
μ	τ	F_u/F_*	F/F_*	%P	F/F_*	%P
0	>5	1.57×10^{-2}	1.00×10^{-1}	−0.9	4.0×10^{-2}	−3.1
0.1	2.2	5.05×10^{-2}	1.37×10^{-1}	−0.5	7.6×10^{-2}	−1.3
0.2	1.7	9.35×10^{-2}	1.85×10^{-1}	−0.1	1.20×10^{-1}	−0.6
0.3	1.4	1.34×10^{-1}	2.30×10^{-1}	0	1.62×10^{-1}	−0.3
0.4	1.2	1.78×10^{-1}	2.78×10^{-1}	0.2	2.08×10^{-1}	−0.1
0.5	1.1	2.24×10^{-1}	3.30×10^{-1}	0.2	2.53×10^{-1}	−0
0.6	0.98	2.72×10^{-1}	3.82×10^{-1}	0.2	3.05×10^{-1}	0
0.7	0.88	3.26×10^{-1}	4.40×10^{-1}	0.2	3.59×10^{-1}	0
0.8	0.78	3.88×10^{-1}	5.05×10^{-1}	0.1	4.22×10^{-1}	0
0.9	0.66	4.70×10^{-1}	5.91×10^{-1}	0.0	5.05×10^{-1}	0
0.975	0	6.02×10^{-1}	7.27×10^{-1}	0	6.40×10^{-1}	0

axis. These features are seen in the Heyer et al. (1990) polarization map of IRAS 16316−1540, a source which has a faint optical nebulosity extending along the blue lobe of the ^{12}CO outflow (Mathieu et al. 1988). Note that the diffuse structure in this model is extremely asymmetric even at low inclination. Generally, the polarization is highest away from the disk plane. Since the source is occulted over many angles and the scattering very asymmetric, the integrated polarization is large as in the streamline case.

3.4. *Other Models*

It is possible to make the extended emission appear significantly brighter relative to the central source with small modifications to the cavity structure. Much of the extended emission arises from distant regions of the cavities, at radii much larger than r_c. At such distances, the streamline boundaries of the cavities are essentially radial. The envelope has substantial optical depth, and so light from the central source impinges on the cavity wall almost tangentially. Limited experiments with the shape of the cavity show that curving the cavity wall even slightly toward the central source can make the wall become several times brighter. The polarization maps give the same general structure as the other hole shapes, however: If there is a cavity, the maps show high polarization in the polar regions, and low polarization in the disk plane. These maps depend on the optical depth through the envelope more than the exact hole shape. The intensity maps tend to show the shape of the hole once the optical depth becomes large.

We also calculated models in which the envelope density distribution was spherically symmetric. With no hole, the images were circularly symmetric. To make direct comparisons to models with cavities, we took the cavity shape to be the same as the streamline cases. The spherically symmetric counterpart to model 5 produced a nearly identical image, though with slight differences of integrated flux and polarization due to the different amounts of extinction with inclination. Thus, the images of model 5, depend almost entirely on the shape of the cavity; if the envelope is opaque, as in model 5, the exact nature of the density distribution is not very important.

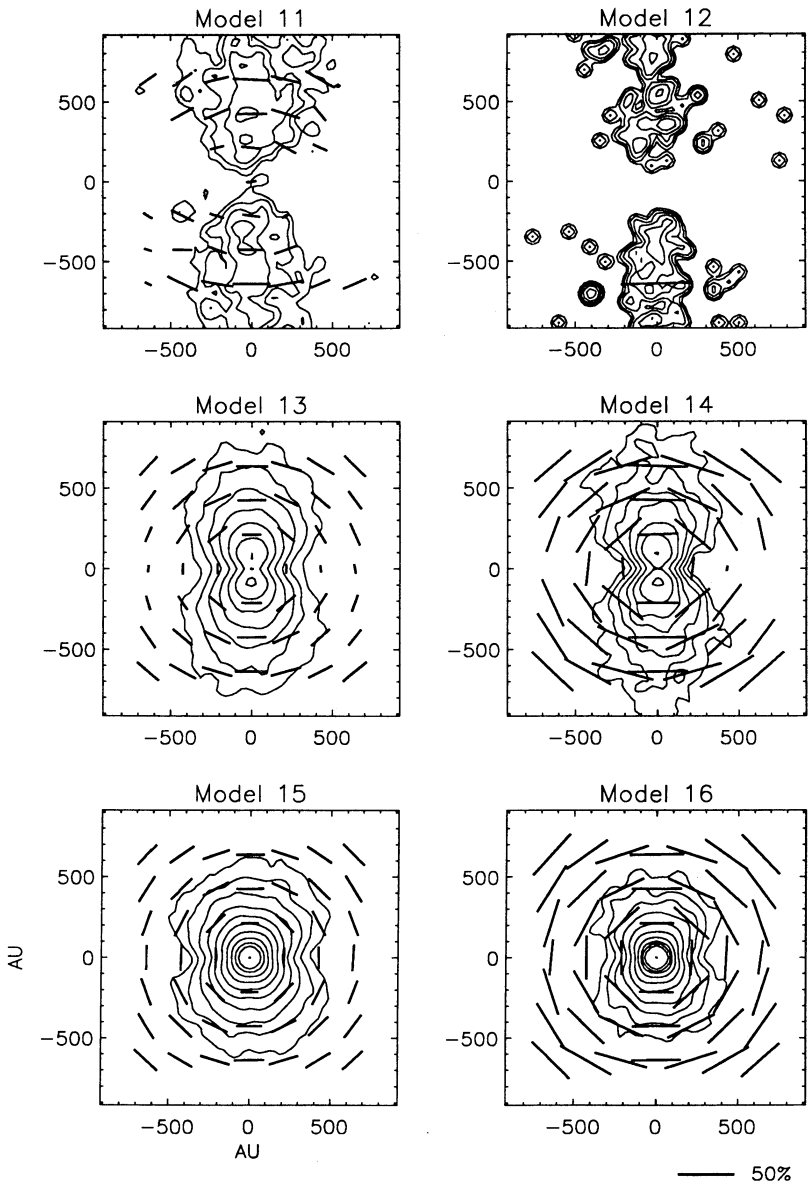

FIG. 4*a*

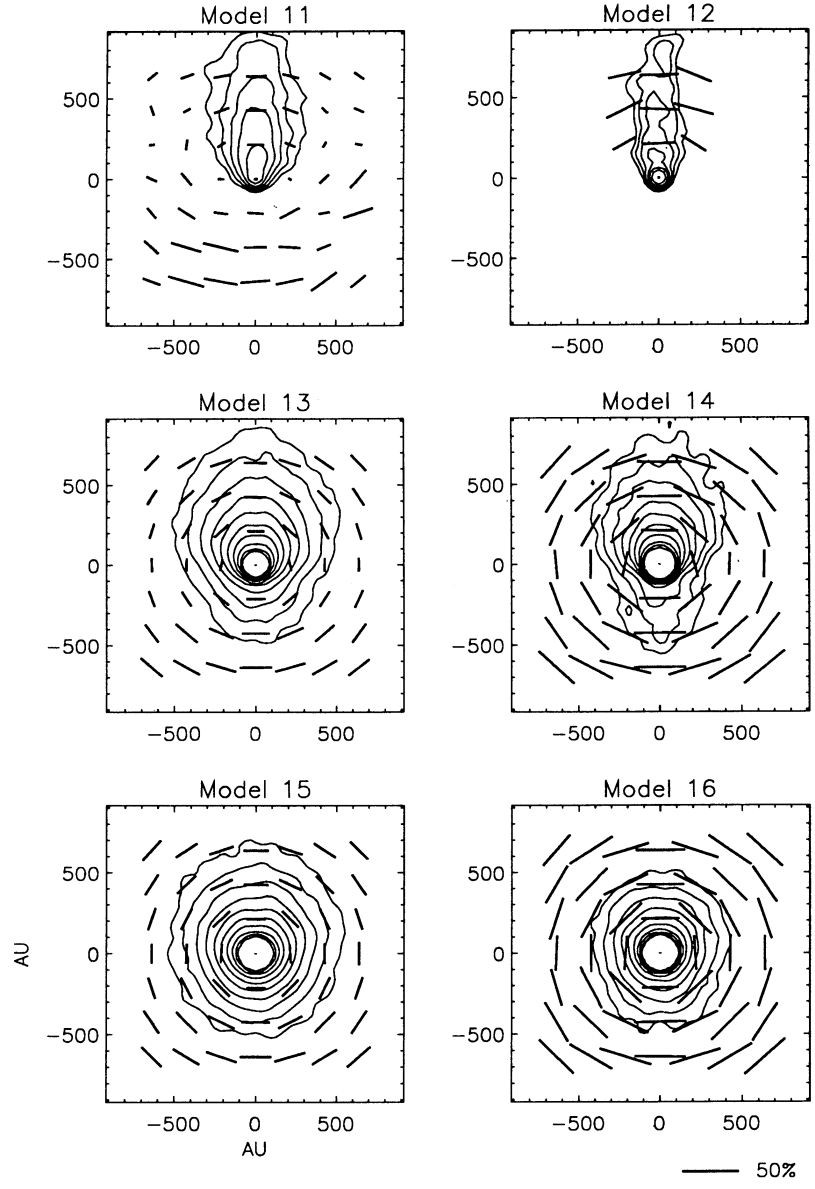

FIG. 4*b*

FIG. 4.—(*a*) Images and polarization maps of a scattering envelope with evacuated polar regions, at inclination $\mu = 0$. The cavity shape is a cylinder of radius 50 AU. Images are convolved with a Gaussian point-spread function of 80 AU and normalized to the peak flux. Contours are spaced by 0.5 mag. The lowest contours of each image are 2×10^{-1}, 1×10^{-1}, 6×10^{-2}, 6×10^{-2}, 5×10^{-3}, and 3×10^{-3}, for models 11, 12, 13, 14, 15, and 16, respectively. (*b*) Same as Fig. 4*a*, with $\mu = 0.6$. The lowest contours are 1×10^{-1}, 5×10^{-2}, 2×10^{-3}, 5×10^{-4}, 4×10^{-4}, and 2×10^{-4}, for models 11, 12, 13, 14, 15, and 16, respectively. (*c*) Same as Fig. 4*a*, with $\mu = 0.9$. The lowest contours are 5×10^{-3}, 1×10^{-3}, 1×10^{-3}, 2×10^{-4}, 2×10^{-4}, and 1×10^{-4}, for models 11, 12, 13, 14, 15, and 16, respectively.

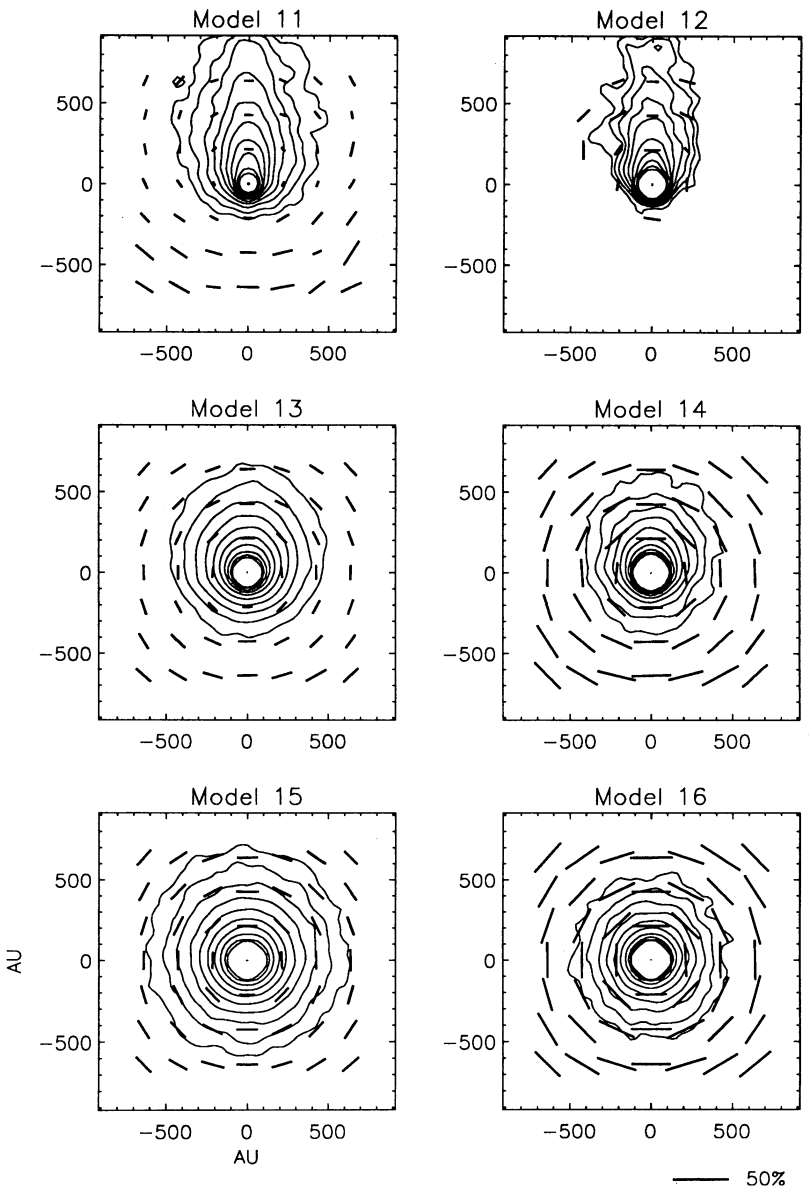

FIG. 4*c*

The images for the less optically thick models do show differences. The spherical envelope (with the same cavity shape) produces more symmetrical images, whereas the rotationally flattened envelope shows the "hourglass" shape.

4. DISCUSSION

4.1. *Disks versus Envelopes*

In Paper I we calculated scattered light distributions for relatively flat disks and showed that such disks are generally extremely faint in comparison with what can be detected in typical observations of the nearest young stellar objects. In contrast, the results of § 3 show that envelope models can be quite bright using physically plausible infall rates. The envelope models are intrinsically brighter because they cover a much larger solid angle as seen from the central source than typical disk models. Moreover, the *apparent* brightness of an envelope model can be much brighter because the envelope obscures the central point source over a much wider range of viewing inclinations than a thin disk. In addition, a rotationally flattened envelope, or an envelope with bipolar cavities, can have enough optical depth at the equator to produce dark lanes, without needing to add a flaring disk. Thus we suggest that many observed reflection nebulae could be (infalling) dusty envelopes rather than disks.

Polarization measurements offer a way to distinguish between disks and envelopes. We showed in Paper I that disk models with realistic properties, as suggested by physical and observational constraints, are likely to be relatively flat ($h/r < 1$) and have a net system polarization *perpendicular* to the disk plane, parallel to the disk axis. Our models of optically thick envelopes have the total system polarization oriented parallel to the disk plane. If the disk rotational axis can be inferred, for example by assuming that it coincides with a high-velocity jet, the disk and (optically thick) envelope models make distinctly different predictions.

In a geometrically thin disk model, the lateral optical depth parallel to the disk plane is much larger than the vertical optical depth through the disk. For typical observational disk parameters (e.g., Beckwith et al. 1990) much of the disk out to ~ 100 AU is vertically optically thick out to wavelengths ~ 100 μm. Therefore, the lateral optical depth of typical disks must be very large in the near-IR. With such an optically thick disk, the scattered light and polarization patterns will change *only* as the albedo and p_{max} of the dust change. It is difficult to understand certain observations in the context of this model. Specifically, some pre–main-sequence objects show a rapid decrease of polarization and of the size of the reflection nebula with increasing wavelength in the near-IR (Hodapp 1984; Monin et al. 1989). For a disk model to explain this, the grains could be small enough to give a decreasing albedo with wavelength as in MRN, but these will give an increase in p_{max} in contradiction with the observations.

In contrast, many of the envelope models discussed here have optical depths along the line of sight ~ 1–5 near 1 μm (models 7–10; see eq. [4]). At these optical depths, a change in opacity of a factor of 2–3, as in going from J band to K band, will decrease the nebular size and polarization in the same manner as the observations, because the stellar flux becomes relatively brighter. Moreover, at longer wavelengths (models 9 and 10), the polarization vector rotates by 90°. Hough et al. (1981) noticed this observational feature in some pre–main-sequence objects. Bastien (1987) concluded that at short wavelengths, scattering in optically thin lobes dominates the polarization, and at longer wavelengths scattering in the disk dominates. In our models we can see the same effect, without appealing to a disk. This effect is not seen in our disk-only models, because at all optical depths the net polarization has the same direction.

4.2. *The "Polarization Disk"*

The polarization maps of several pre–main-sequence objects have what is called a "polarization disk," in which the polarization clearly departs from a centrosymmetric pattern; the polarization vectors are essentially parallel through a band near the source. Objects which exhibit this behavior include NGC 2261/R Mon (Warren-Smith, Draper, & Scarrott 1987; Aspin, McLean, & Coyne 1985; Scarrott, Draper, & Warren-Smith 1989; Minchin et al. 1991), L1551 IRS 5 (Lenzen 1987; Scarrott 1988; Draper, Warren-Smith, & Scarrott 1985b), PV Cep (Gledhill, Warren-Smith, & Scarrott 1987), and R and T CrA (Ward-Thompson, Warren-Smith, & Scarrott 1985). Other objects, such as Par 21 (Draper, Warren-Smith, & Scarrott 1985a) and HL Tau (Gledhill & Scarrott 1989), show elliptical polarization patterns or a band of null vectors. A more detailed listing of polarization maps is given in Bastien & Ménard (1990).

One explanation of the "polarization disk" feature is in terms of grains organized in a disk or a large toroidal structure and aligned by a magnetic field. No quantitative models have been presented for this process. Bastien & Ménard (1990) list several arguments against the aligned grain model. An alternative model was proposed by Bastien & Ménard (1988, 1990), who suggested that a disk with appropriate scattering geometry could produce the required pattern of polarization. They calculated models in which photons scattered twice, above and below the disk plane in specific locations, and they were able to produce a pattern of aligned vectors.

In Paper I we considered polarization patterns from scattering disks with physically plausible parameters for pre–main-sequence objects. We found generally centrosymmetric patterns, unlike Bastien & Ménard. The dark equatorial band in our flared images (Paper I, Figs. 6–8) would probably show the parallel vectors in the edge-on case at high spatial resolution (about 5 AU in a 100 AU disk), but we do not have enough signal-to-noise ratio in this region to decide the question. In a large, tenuous disk (such as Paper I, Fig. 9), though the optical depth through the equator can be much greater than 1, the polarization vectors in the midplane are perpendicular to the disk plane, because the light which dominates the flux is singly scattered from the tenuous upper regions. Because the net polarization from a disk is perpendicular to the disk plane, very high resolution is required to resolve the parallel vectors that result in the darkened midplane due to multiple scattering.

As shown in Figure 3*a*, the optically thick envelope with a hole viewed edge-on produces this pattern of parallel vectors in the darkened equatorial band. Because the albedo of the grains is relatively low, the polarization is due mostly to single or double scattering. The asymmetric geometry at high optical depth just changes the *path* of the photons. A simple scattering geometry results for scattering into $\mu \sim 0$: Most photons emerging from the polar regions have scattered once, and the position angle there is perpendicular to the plane of scatter, or parallel to the disk plane. Most photons emerging from the equatorial region have scattered twice (none has scattered once), first above in the polar region and then back down to the equatorial region—essentially scattering *around* the opaque equatorial region, not *through* it. The resulting polarization position angle is also parallel to the disk plane.

One important point to keep in mind is that many published polarization maps extend over very large scales, to thousands of AU or more, with pixel sizes of several hundred AU. Therefore, we recomputed images of larger size using the parameters of model 5, and these are shown in Figure 5. The polarization vectors are clearly parallel along the equatorial plane at high inclination ($\mu = 0$–0.3), very suggestive of the "polarization disk." The disk itself is extremely small compared to the image dimensions and therefore is not responsible for the polarization pattern. Our "polarization disk" *results entirely from scattering in the envelope.* Comparison with Figure 3 shows that the "polarization disk" is apparent even at low resolution. Photons from above and below the dark equatorial band contribute to the flux in a pixel centered in the middle. The parallel vectors could in fact be mostly due to single scattering from the region where photons can escape, which at low resolution appear to come from the central region. Thus, the low-resolution polarization maps may just reflect the orientation of the singly scattered vectors above and below the opaque equatorial region.

5. COMPARISON WITH SPECIFIC OBJECTS

In subsequent papers we will construct models in an attempt to reproduce the observations of specific objects. Here we consider the applicability of our general results in two well-known cases; R Mon, which appears to have a wind-driven cavity observed at high inclination, and T Tau, which may be a case of a pre–main-sequence object observed down the evacuated wind cavity.

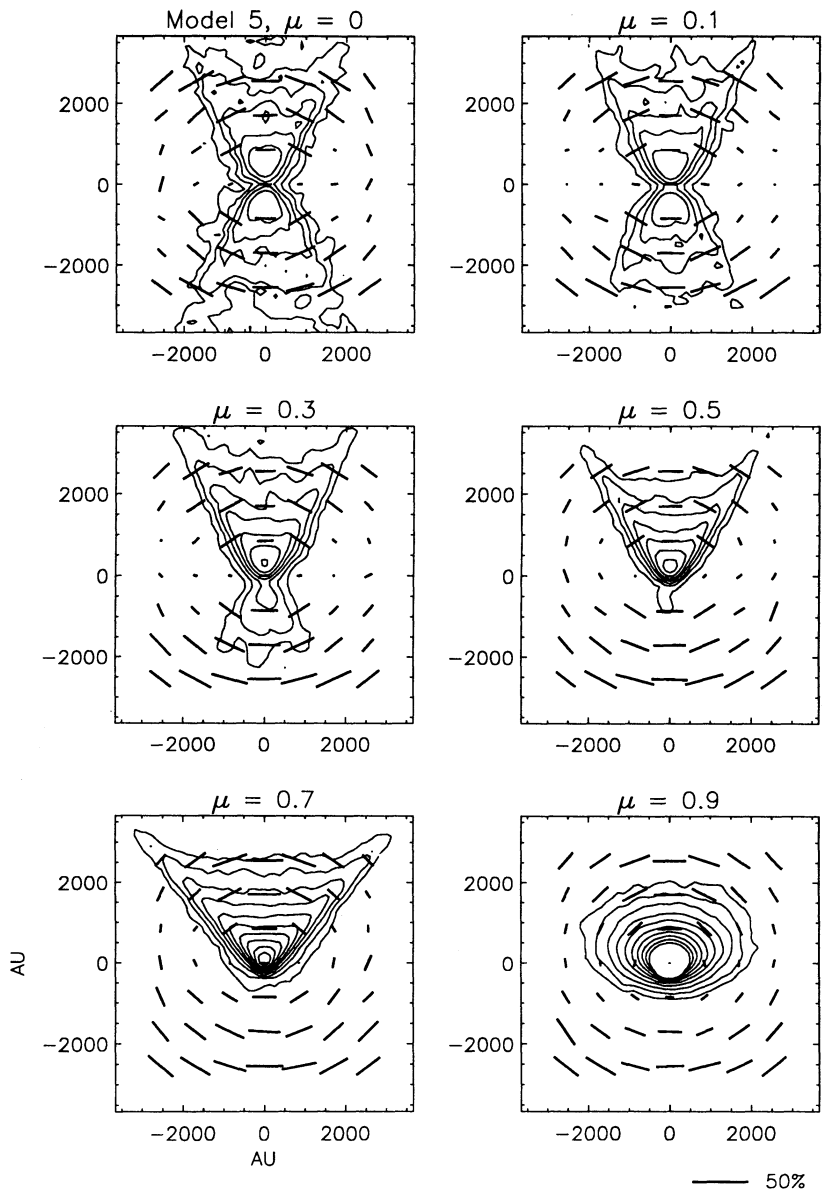

FIG. 5.—Images of model 5, an envelope with a streamline hole, shown at larger scale. Images are convolved with a Gaussian point-spread function of 240 AU, and normalized to the peak flux. The contours are separated by 0.5 mag intervals. The lowest contours are 1×10^{-1}, 1×10^{-1}, 6×10^{-2}, 5×10^{-2}, 1×10^{-2}, and 3×10^{-5}, for $\mu = 0, 0.1, 0.3, 0.5, 0.7$, and 0.9, respectively.

5.1. *R Mon*

The pre–main-sequence object R Mon is surrounded by a bright optical reflection nebula which is "cometary" in shape. Minchin et al. (1991) imaged R Mon in the near-IR and found that the polarization in an 8″ diameter aperture decreases from 11% at J to 8.5% at H to 5.6% at K. Our models indicate that the envelope must be optically thick at K to produce such large polarization. In our streamline hole model at $\mu \sim 0.3$, to get 5% polarization requires an optical depth of at least 5. Using Table 1, scaling model 8 to K-band opacity ($\kappa \sim 25$ cm^2 g^{-1}) implies an infall rate of $6 \times 10^{-6}(M/0.5\ M_\odot)^{1/2}(r_c/100\ \mathrm{AU})^{1/2}$ $M_\odot$ yr^{-1} for a 0.5 $M_\odot$ core. A cylindrical hole also gives a shape similar to R Mon over a range of inclinations.

The near-IR polarimetry maps of R Mon show the pattern becoming more circular at shorter wavelength, as our model show (Figs. 3*a*, 4*a*). The observed K-band intensity image shows an equatorial pinching, also apparent in model 8 (e.g., Fig. 3*a*). At lower optical depths (Fig. 3*a*, bottom), the pinching goes away, as does the polarization, again indicating that the observed K-band image is more opaque than this.

Our map of model 5 $\mu = 0.3$ qualitatively resembles the visual-wavelength maps of R Mon as shown in Figure 6; the polarization bin size in the Warren-Smith et al. (1987) map is 2.″5 × 2.″5, corresponding to 2000 AU × 2000 AU at a distance of 800 pc. The polarization in the middle pixel of this map is 13%, oriented parallel to the disk plane. The model 5 $\mu = 0.3$ image integrated over the same area results in 12% polarization. We suggest that this pattern of parallel polarization results from poor resolution of the envelope rather than in a

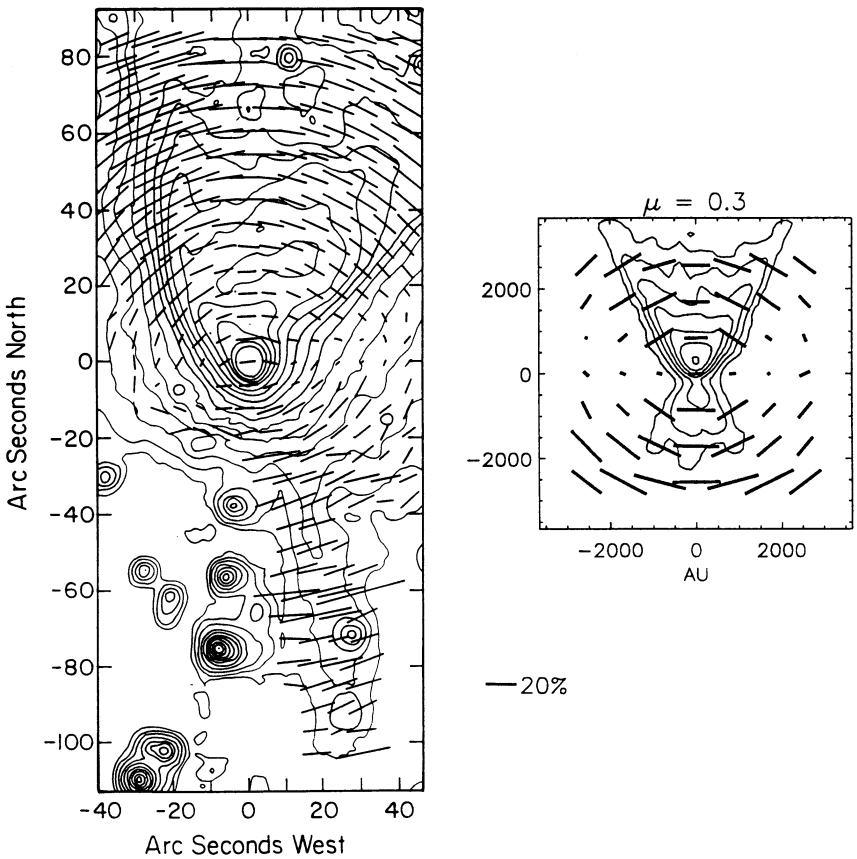

FIG. 6.—On the left is an *R*-band linear polarization map of the R Mon/NGC 2261 system, from Warren-Smith et al. (1987). On the right is an image from model 5 (Fig. 5). In both images, the contours are spaced by 0.5 mag. The polarization factors have the same scale, shown at bottom right.

physical disk, a suggestion which is supported by the large scales involved and the resolved structure of the nebula.

5.2. *T Tau*

The prototypical pre–main-sequence star T Tauri has modest line-of-sight extinction ($A_V \approx 1.4$; Cohen & Kuhi 1979), yet it has a large IR excess and is surrounded by a scattered light nebula (Weintraub et al. 1992). T Tau is double; the optical star has an IR companion of comparable luminosity separated by about 0.″7. The spectral energy distribution of the IR companion peaks near 5 μm, also suggesting the presence of substantial dust extinction (Ghez et al. 1991).

Weintraub et al. (1992) imaged T Tau at near-IR wavelengths (*J* and *K*) using an occulting mask. The near-IR images are roughly circular; the south and west quadrants are approximately 4 times brighter than the north and east quadrants at *K*. The polarization maps are approximately centrosymmetric. The surface brightness of the envelope *F* falls off with distance *r* from the source as a power law, $F \sim r^{-n}$, where *n* is ~ 2.6 at *J* and ~ 2.4 at *K*. Assuming that the scattering nebula is optically thin, Weintraub et al. calculated that the density in the nebula falls off with increasing radius as $\rho \sim r^{-1.5}$, consistent with the density distribution expected for an infalling envelope. However, it seems likely that the nebula is not optically thin at *J* (1.25 μm), because the nebular surface brightness at *J* and *K* (2.2 μm) are almost the same, and this is difficult to reconcile with the large opacity difference usually inferred between these two wavelengths (cf. Savage & Mathis 1979; MRN). From an analysis of the *K*-band image, Weintraub et al. (1992) concluded that T Tau is surrounded by a flattened distribution of dust, with an estimated envelope mass (gas and dust) of 0.03 $M_\odot$ between 400 and 1400 AU. They suggest that this nebula is probably an infalling envelope or a large disk.

The optical component of T Tau is probably observed nearly pole-on. Herbst et al. (1986) found variability of T Tau with a 2.8 day period, which they attributed to rotational modulation by starspots. Combining this period with the observed projected rotational velocity and with radius estimates for the star, Herbst et al. were able to show that the inclination of the optical star is probably between $8° < i < 13°$. If the stellar rotational axis is aligned with the disk rotational axis, then we could be observing T Tau along a polar cavity in a dusty envelope, which would explain the low line-of-sight extinction combined with the large infrared excess. This picture also explains the roughly circular isophotes and centrosymmetric polarization pattern in the near-IR (Weintraub et al. 1992). We therefore compare our $\mu = 1$ models to T Tau. We consider the scattered light distribution only at distances substantially larger than the binary separation of 0.″7, and ignore the possible complications of two light sources.

Figure 7 shows the pole-on model results. The data are binned to 0.″71 pixels for comparison to the observations of T Tau. We place the stellar flux into the middle pixel, as Weintraub et al. did. The flux variations with radius are de-

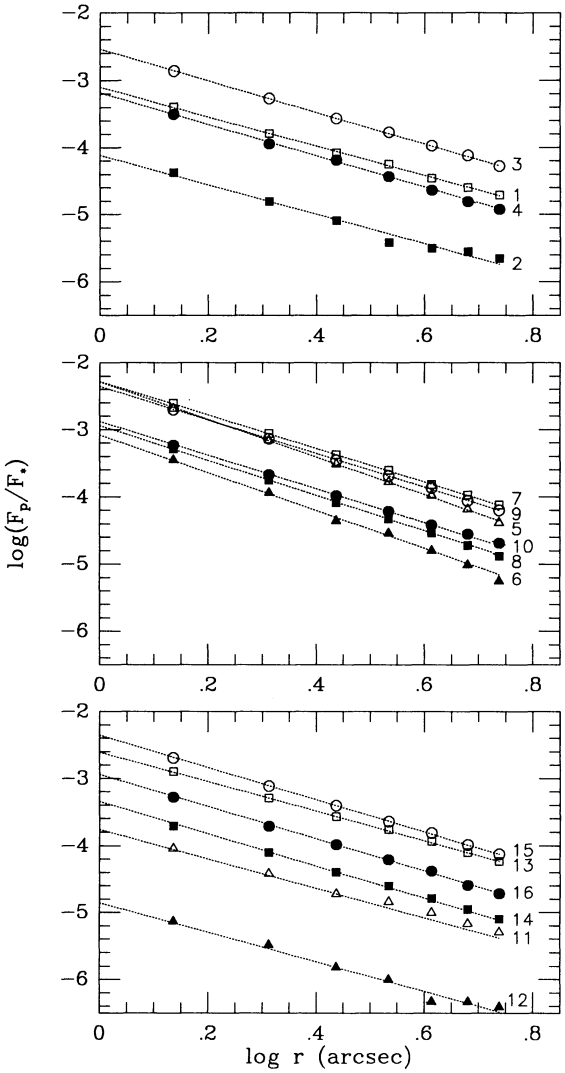

FIG. 7.—Flux as a function of distance from the central source for the envelope models without holes. The flux per pixel F_p is normalized to the stellar flux which is summed in the middle pixel. The model numbers (Table 1) are shown on the right. The dotted lines are power-law fits, whose exponents are given in Table 5.

scribed with power laws with exponent n shown in Table 5. In the models without holes, the decrease of intensity with radius is shallower, with n between 2 and 2.35. In the models with streamline holes, n is about 2.5 at lower optical depths and 2.8 at higher. The flux falls off more rapidly at high optical depth because the surface of the hole is nearly radial, so starlight impinges nearly tangentially. A parabolic hole with the same opening angle, all other parameters remaining the same, gives $n = 2$. The cylindrical hole models have a slope of 2.2 in the optically thick cases, and 2.4 in the optically thin models (models 15 and 16).

The flared-disk models from Paper I have a slope of 2, but a factor of 10 less flux scatters from the disks at such large distances from the star. In addition, unless the vertical optical thickness of the flared disk remains large at large radii, implying a mass greater than 0.5 $M_\odot$, the effective scattering surface curves back down to the midplane and the scattered flux will drop dramatically at this distance.

TABLE 5

MODEL RESULTS

Model	Flux vs. Radius Exponent	Average Number of Scatters
1	2.2	2.2
2	2.2	1.3
3	2.35	1.5
4	2.35	1.2
5	2.8	1.6
6	2.8	1.2
7	2.5	1.6
8	2.5	1.2
9	2.5	1.4
10	2.5	1.1
11	2	2.1
12	2.2	1.3
13	2.2	1.7
14	2.3	1.2
15	2.4	1.4
16	2.4	1.1
Parabolic hole	2	1.7

The models that agree best with the T Tau observations are models 5, 7, and 9. These give the most flux, yet they still fall below the observations. A higher albedo, narrower hole, or slightly more curvature in the hole would increase the flux. Models 7 and 9 give similar slopes to those observed in T Tau ($n \sim 2.5$), and nearly indistinguishable results when compared to each other. Yet, the optical depths vary by a factor of 3 between the models. Model 5 actually falls below the other two. In the optically thick case, the surface brightness does not directly constrain the density law, but is more dependent upon the shape of the scattering surface.

In Figure 8 we show models 7 and 9 compared with the observations of T Tau by Weintraub et al. (1992). Both of these envelopes have large lateral optical thicknesses, but model 9 has $\tau \sim 1$ through the envelope to the source over a range of intermediate inclinations (Table 3). The opacities are such that models 7 and 9 could correspond to the J- and K-band images, assuming a higher albedo at K than MRN dust has. Pendleton et al. (1990) argue that large grains in star-forming regions will keep the albedo high in the IR so this may not raise serious objections. Model 10 gives the same *scattering* vertical optical

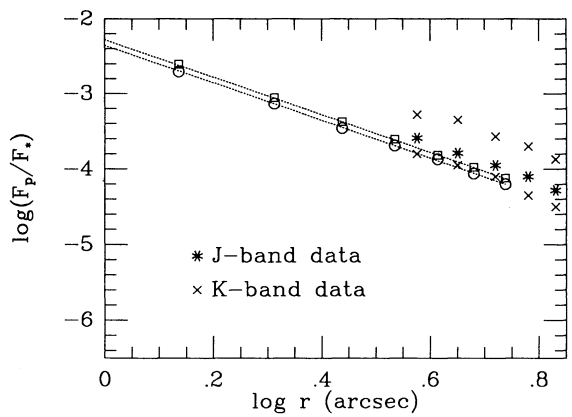

FIG. 8.—Flux as a function of distance from the central source for the best-fitting envelope models (models 7 and 9), and the data. The J-band data are an average over the north and east quadrants. The K-band data are averaged north–east (the lower points) and south–west (upper).

depth as Weintraub et al. estimated for the K-band image, but model 9, with its higher albedo, agrees better with the data. The vertical optical depth (all the way through) in model 7 at 420 AU is $\tau \sim 2$, larger than the estimate of Weintraub et al. The models agree well with the observed north and east quadrants; the K-band image is low compared to the other quadrants. A model with slight inclination, and perhaps allowing more scattering by having the hole slightly curved, may fit the data better.

To check that an optically thin model does not give more flux, we computed a model with ~ 6 times less optical depth than model 9 giving a lateral optical depth of $\tau = 1$. The resulting surface brightness distribution also followed the $n = 2.5$ power law, but the level decreased by a factor of 4 compared to model 9.

The Weintraub et al. polarization maps show higher values in the northeast quadrants than in the southwest at K. This effect appears in the models as well, if the object is slightly inclined, as in Figure 3*c*, where $\mu = 0.9$. The observed polarization vector values range from 3% to 40%. The model values range from 0 to 35%, in models 7 and 9. Models 8 and 10 have polarizations closer to 50%. These are all close enough to the observations that it would be difficult to distinguish grain models based on the polarization. The integrated polarization of T Tau is 1.2% at V and 0.5% at K but rotated by 90° at K (Hough et al. 1981). This position angle rotation happens between the H-band and K-band. Our models produce such a rotation and imply that the envelope is optically thick at J (§ 3.2), and less thick at K.

We conclude that the observations of near-IR scattered light in T Tau are best explained if the envelope becomes optically thick at J, since the amount of scattered light does not increase with increasing scattering opacity. In addition, the albedo at K may be higher than MRN grains give. If model 7 corresponds to the J-band wavelength, the infall rate is $\dot{M} = 2.1 \times 10^{-6}$, and mass of the envelope in the radius range 400 to 1400 AU is $\sim 0.01\ M_{\odot}$. Since we have just made general comparisons to models presented here, we do not claim accuracy to better than a factor of 5 in the mass. Overall, our envelope mass and geometry are in reasonable agreement with the Weintraub et al. estimates.

Our results, which require the envelope of T Tau to be optically thick in the near-IR, have interesting implications for the spectral energy distributions. The speckle results of Ghez et al. (1991) suggest that, even after accounting for the infrared companion, the near- to mid-IR spectral energy distribution of the optical primary is flatter than expected from simple disk models (Kenyon & Hartmann 1987). However, an absorbing envelope of substantial optical depth, covering an appreciable solid angle as seen from the star, could easily produce significant IR excess emission (Kenyon & Hartmann 1991). Moreover, the envelope could conceivably be responsible for the extinction of the IR companion. The spectral energy distribution derived by Ghez et al. (1991) for the secondary peaks at ~ 5 μm, suggesting ~ 5 mag of extinction at J. In model 7, the optical depth along the z direction to a source 100 AU from the center is $\tau = 2$. Given the uncertainties involved in this calculation, the level of agreement suggests that an envelope of the type considered here could well explain the extinction of the secondary star.

6. CONCLUSIONS

We have presented models of light scattering from dusty envelopes around young stellar objects. Although we have adopted specific geometries for these envelopes, the following general conclusions can be drawn from the models.

1. An infalling envelope can easily be much brighter in scattered light than physically plausible disks. For this reason, we suggest that many reflection nebulae have been incorrectly interpreted as scattering from a disk (see also Paper I).

2. High polarization in some regions of the nebula implies single scattering in those regions, but this does not necessarily imply an optically thin envelope. For grain albedos near $\omega \sim 0.5$, the average number of scatters will be ≤ 2, even in optically thick envelopes. In addition, single scattering can occur along the walls of the (presumably wind-driven) cavity in an optically thick nebula.

3. In models with bipolar cavities, the polarization integrated over the image area is high ($\gtrsim 3\%$) over a large range of inclination when the central unpolarized source is extincted by $\gtrsim 5$ mag along the line of sight.

4. The polarization position angle can distinguish between envelopes and disks. For disks, the net system polarization is parallel to the rotation axis, perpendicular to the disk plane; for optically thick envelopes with rotation or wind-driven holes, the reverse is true since more singly scattered light escapes from the polar regions. The models predict that the angle of polarization should rotate by 90° as the envelope becomes optically thin at longer wavelengths. This happens at a shorter wavelength if the envelope has bipolar cavities than if it does not.

5. So-called "polarization disks," such as seen in R Mon, can be produced by scattering envelopes with bipolar cavities, without any need for a large disk. Since many observed "polarization disks" are very large (10^3–10^4 AU), much larger than disk dimensions derived from other techniques (e.g., Beckwith et al. 1990), and are comparable to the expected size of the natal molecular cloud core, the envelope explanation is generally more plausible. In addition, the parallel vectors arising from the envelope model can be seen at low resolution, since the polarization above and below the equatorial region is in the same direction. Parallel vectors can arise in the midplane of a large flared disk (Bastien & Ménard 1988) but must be observed at high resolution or the brighter flux above and below the midplane will dominate with its position angle perpendicular to the disk plane.

6. The polarization patterns provide clues about geometry and dust properties. In models without holes, the patterns tend to be centrosymmetric, with slightly higher polarization in the polar regions. Models with higher optical depths than we calculated may show more asymmetric patterns, but we did not have the signal-to-noise ratio to make the calculations.

The models with holes show very asymmetric patterns if the envelope is optically thick ($\tau \geq 10$ over a range of inclinations). In the equatorial region, the polarization vectors are reasonably large ($\sim 10\%$) and aligned parallel to the disk plane if the envelope is viewed nearly edge-on (§ 4.2). At lower inclinations ($\mu \sim 0.4$–0.8), the equatorial region shows a null pattern and high polarization appears in the polar regions. If the polarization is higher in the more obscured lobe, the grains are forward-throwing (§ 3.2) (if the dust is axisymmetrically distributed). The envelope with a cylindrical hole produces polarization vectors parallel to the disk plane over a large area of the image. When viewed nearly pole-on, the pattern is distinctive, with several perpendicular vectors along the upper lobe and all parallel vectors in the lower lobe.

7. Intensity maps of scattered light in optically thick envelopes with holes delineate the hole shape. At lower optical

depths, the intensity maps probe density structure. Modeling multiwavelength observations could constrain both outflow cavity shapes and envelope densities.

8. "Protostars," that is, objects with high mass infall rates $\sim 10^{-6}\ M_{\odot}\ \mathrm{yr}^{-1}$ can be detected at optical wavelengths if the angular momentum of the collapsing material causes it to fall to disk radii of ~ 100 AU. Protostars with less angular momentum and thus infall to much smaller radii can also be detected at optical wavelengths if bipolar cavities are created in the envelope by powerful pre–main-sequence winds.

We thank Scott Kenyon for useful comments. This work was supported by NASA grants NAGW-2919 and NAGW-2306 to the Smithsonian Astrophysical Observatory.

REFERENCES

Adams, F. C., Emerson, J. P., & Fuller, G. A. 1990, ApJ, 357, 606
Adams, F. C., Lada, C., & Shu, F. H. 1987, ApJ, 312, 788
Aspin, C., McLean, I. S., & Coyne, G. V. 1985, A&A, 149, 158
Barsony, M., & Kenyon, S. J. 1992, ApJ, 384, L53
Bastien, P. 1987, ApJ, 317, 231
Bastien, P., & Ménard, F. 1988, ApJ, 326, 334
———. 1990, ApJ, 364, 232
Beckwith, S. V. W., Sargent, A. I., Chini, R. S., & Gusten, R. 1990, AJ, 99, 924
Beckwith, S. V. W., Sargent, A. I., Koresko, C. D., & Weintraub, D. A. 1989, ApJ, 343, 393
Cassen, P., & Moosman, A. 1981, Icarus, 48, 353
Chandrasekhar, S. 1960, Radiative Transfer (New York: Dover)
Chevalier, R. A. 1983, ApJ, 263, 753
Cohen, M., & Kuhi, L. V. 1979, ApJS, 41, 743
Draper, P. W., Warren-Smith, R. F., & Scarrott, S. M. 1985a, MNRAS, 212, 1P
———. 1985b, MNRAS, 216, 7P
Edwards, S., Ray, T., & Mundt, R. 1991, Protostars and Planets III, ed. E. H. Levy & J. Lunine (Tucson: Univ. of Arizona Press), in press
Ghez, A. M., Neugebauer, G., Gorham, P. W., Haniff, C. A., Kulkarni, S. R., & Matthews, K. 1991, AJ, 102, 2066
Gledhill, T. M., & Scarrott, S. M. 1989, MNRAS, 236, 139
Gledhill, T. M., Warren-Smith, R. F., & Scarrott, S. M. 1987, MNRAS, 229, 643
Grasdalen, G. L., Sloan, G., Stout, N., Strom, S. E., & Welty, A. D. 1989, ApJ, 339, L37
Herbst, W., Booth, J. F., Chugainov, P. F., Zajtseva, G. V., Barksdale, W., Covino, E., Terrenegra, L., Vittone, A., & Vrba, F. 1986, ApJ, 310, L71
Heyer, M. H., Ladd, E. F., Myers, P. C., & Campbell, N. 1990, AJ, 99, 1585
Heyer, M. H., Snell, R. L., Goldsmith, P. F., & Myers, P. C. 1987, ApJ, 321, 370
Hodapp, K.-W. 1984, A&A, 141, 255
Hough, J. H., Bailey, J., Cunningham, E. C., McCall, A., & Axon, D. J. 1981, MNRAS, 195, 429
Kenyon, S. J., & Hartmann, L. 1987, ApJ, 323, 714
Kenyon, S. J., & Hartmann, L. 1991, ApJ, 383, 664
Larson, R. B. 1969, MNRAS, 145, 271
———. 1972, MNRAS, 157, 121
Lazareff, B., Pudritz, R. E., & Monin, J.-L. 1990, ApJ, 358, 170
Lenzen, R. 1987, A&A, 173, 124
Lin, D. N., & Pringle, J. E. 1990, ApJ, 358, 515
Mathieu, R. D., Benson, P. J., Fuller, G. A., Myers, P. C., & Schild, R. E. 1988, ApJ., 330, 385
Mathis, J. S., Rumpl, W., & Nordsieck, K. H. 1977, ApJ, 217, 425 (MRN)
Minchin, N. R., Hough, J. H., McCall, A., Aspin, C., Yamashita, T., & Burton, M. G. 1991, MNRAS, 249, 707
Monin, J.L., Pudritz, R. E., Rouan, D., & Lacombe, F. 1989, A&A, 215, L1
Pendleton, Y., Tielens, A. G. G. M., & Werner, M. W. 1990, ApJ, 349, 107
Savage, B. D., & Mathis, J. S. 1979, ARA&A, 17, 73
Scarrott, S. M. 1988, MNRAS, 231, 39P
Scarrott, S. M., Draper, P. W., & Warren-Smith, R. F. 1989, MNRAS, 237, 621
Shu, F. H. 1977, ApJ, 214, 488
Shu, F. H., Adams, F. C., & Lizano, S. 1987, ARA&A, 25, 23
Strom, K. M., Strom, S. E., Edwards, S., Cabrit, S., & Skrutskie, M. F. 1989, AJ, 97, 1451
Terebey, S., Shu, F. H., Cassen, P. 1984, ApJ, 286, 529
Terebey, S., Vogel, S. N., & Myers, P. C. 1989, ApJ, 340, 472
Ulrich, R. K. 1976, ApJ, 210, 377
Ward-Thompson, D., Warren-Smith, R. F., & Scarrott, S. M. 1985, MNRAS, 215, 537
Warren-Smith, R. F., Draper, P. W., & Scarrott, S. M. 1987, ApJ, 315, 500
Weintraub, D. A., Kastner, J. H., Zuckerman, B., & Gatley, I. 1992, ApJ, 391, 784
White, R. L. 1979, ApJ, 229, 954
Whitney, B. A., & Hartmann, L. 1992, ApJ, 395, 529
Witt, A. N. 1989, in Interstellar Dust, ed. L. J. Allamandola & A. G. G. M. Tielens (Dordrecht: Kluwer)